

Rhodium–Tin Binary Nanoparticle—A Strategy to Develop an Alternative Electrocatalyst for Oxygen Reduction

Minjeh Ahn,[†] In Young Cha,[‡] Jinwon Cho,[†] Hyung Chul Ham,[†] Yung-Eun Sung,^{*,§,¶} and Sung Jong Yoo^{*,†,Δ}

[†]Fuel Cell Research Center, Korea Institute of Science and Technology, Seoul, 02792, Republic of Korea

[‡]Research Park, LG Chem, Daejeon, 34122, Republic of Korea

[§]School of Chemical and Biological Engineering, Seoul National University, Seoul, 08826, Republic of Korea

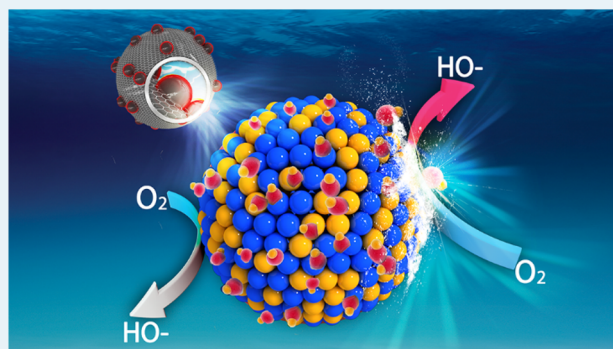
[¶]Center for Nanoparticle Research, Institute for Basic Science, Seoul, 08826, Republic of Korea

^ΔDivision of Energy & Environment Technology, KIST-School, Korea University of Science and Technology, Daejeon, 34113, Republic of Korea

Supporting Information

ABSTRACT: A Rh–Sn nanoparticle is achieved by combinatorial approaches for application as an active and stable electrocatalyst in the oxygen reduction reaction. Both metallic Rh and metallic Sn exhibit activities too low to be utilized for electrocatalytic reduction of oxygen. However, a clean and active Rh surface can be activated by incorporation of Sn into a Rh nanoparticle through the combined effects of lateral repulsion, bifunctional mechanism, and electronic modification. The corrosion-resistant property of Rh contributes to the construction of a stable catalyst that can be used under harsh fuel cell conditions. Based on both theoretical and experimental research, Rh–Sn nanoparticle designs with inexpensive materials can be a potential alternative catalyst in terms of the economic feasibility of commercialization and its facile and simple surfactant-free microwave-assisted synthesis.

KEYWORDS: electrocatalyst, oxygen reduction, fuel cells, rhodium–tin, nanomaterial



Electrocatalysis for the oxygen reduction reaction (ORR) has been extensively researched in the fields of nanomaterials and electrochemistry, using polymer electrolyte membrane fuel cells, owing to the sluggish kinetics of ORR compared to the hydrogen oxidation reaction.^{1,2} Nanosized materials for ORR catalysis should be chemically active toward oxygen molecules and stable under the corrosive operating conditions of a fuel cell system. Noble metals (e.g., Pt, Pd, etc.) have been suggested as electrocatalysts that satisfy the minimum requirements of ORR activity and material stability.^{3–5} In terms of the basic aspects of surface chemistry, the ORR mechanism involves the adsorption of an oxygen molecule, stabilization of hydroxyl functional groups on the catalyst surface, and subsequent desorption of water molecule from the active metal surface.^{6,7} This implies an optimum binding energy between the oxygen species and the metal surface for feasible ORR. Theoretical calculations have revealed that a relatively lower binding energy barrier of oxygen and its related species on Pt surface leads to higher coverage of adsorbed oxygen species on the Pt surface that hampers ORR by blocking the active sites.^{8–10} Therefore, Pt- and Pd-based nanoparticles alloyed with 3d transition metals like Ni, Co, Fe, and Cu have been designed for enhancing the ORR kinetics by

tuning the oxygen binding energy and by reducing the amounts of expensive noble metals used.^{11–14} Insertion of 3d transition metal atoms into Pt or Pd nanoparticles can induce a small lattice mismatch in the crystal structure, which alters the electron density of Pt or Pd such that optimum interaction energy with oxygen adsorbates is further approached.

Both ORR activity and economic feasibility can be improved through incorporation of 3d transition metals. However, stability of the resultant alloys is a serious issue because the 3d transition metal is prone to dissolution under harsh operating conditions.^{15–17} To fulfill the requirements of both high activity and long-term stability for bimetallic nanoparticles, incorporation of a third metal component has been proposed (e.g., Au, Rh, and Mo).^{18–20} Ternary electrocatalysts maintained their ORR activities after accelerated degradation tests due to the extremely high material stability of the third metal atoms. However, these designs require complicated procedures and further treatments to obtain appropriate compositions and local sites on the surface of the nanomaterials. Moreover, from the viewpoint of expansion of material

Received: July 19, 2017

Published: August 3, 2017

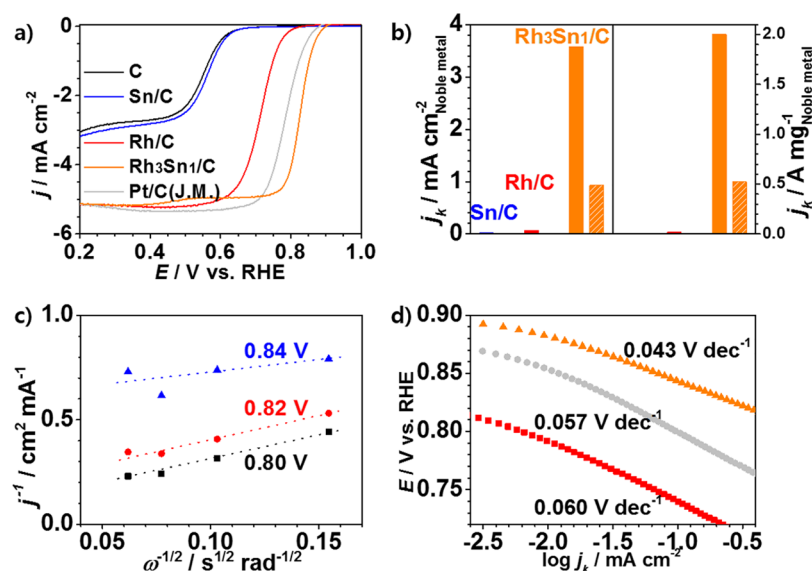


Figure 1. Electrocatalysis of Rh–Sn nanoparticles. (a) Linear sweep voltammograms of Rh- and Sn-based catalysts and commercial Pt/C in an oxygen-saturated 0.1 M potassium hydroxide at room temperature with a rotating speed of 1,600 rpm and a sweep rate of 5 mV s⁻¹. (b) Comparison of kinetic current densities normalized by the electrochemical active surface area and weight of total noble metals at 0.75 V (left side) and 0.80 V (right side). (c) The Koutecky–Levich plots obtained from ORR results of Rh₃Sn₁/C at various potentials and rotating speeds. (d) Comparison of Tafel slopes for Rh₃Sn₁/C (orange triangle), Rh/C (red rectangular), and commercial Pt/C (gray circle) catalysts.

selection for ORR electrocatalyst excluding conventional Pt- and Pd-based materials, it is essential to exploit new candidates for relieving the dependence of specific materials and suggesting insights to develop active nanomaterials. Since monometallic Au or Rh nanoparticles have poor ORR activities even in an alkaline electrolyte, morphology-controlled Pt-free binary nanostructures like Pd–Rh and Au–Rh have been proposed to promote ORR activity for highly stable and durable catalysis.^{21–24} It signifies that Rh-based materials may be possible candidates for ORR electrocatalyst via adequate combinatorial design. Despite these efforts, cost issues still remain. Therefore, new designs of nanomaterials for electrocatalytic reactions are in demand to produce active and stable ORR catalysts suitable for industrial applications.

Sn is a cheap material that is known to serve as an effective cocatalyst for electrocatalysts, especially in ethanol oxidation. Sn-incorporated Pt or Pd nanoparticles displayed better catalytic activities because of the bifunctional effect and electronic modification on the nanoparticle surface.^{25,26} Initial research in the field of electrocatalysis revealed that the Pt–Sn catalyst showed enhanced performance toward alcohol oxidation compared to Pt itself, whereas Ir–Sn and Rh–Sn had no effect and a negative effect due to the low activities of Ir and Rh, respectively.^{27,28} However, by controlling the operating conditions and carefully tailoring the nanoparticle geometry, few studies recently reported that these nanomaterials were also successfully applied as effective catalysts for ethanol oxidation.^{29,30} Likewise, these combinatorial-designing approaches can lead to other electrocatalytic reactions including ORR.³¹ Rh has been widely utilized in the fields of alcohol electrooxidation, water splitting, and exhaust gas purification due to its unique binding properties and high corrosion resistance.^{32,33} Thus, the problem of corrosion-induced instability of the ORR catalysts can be solved by using Rh-based bimetallic nanoparticles.

From these perspectives, a new type of Rh–Sn bimetallic nanoparticle has been developed as an exceptionally active and

stable electrocatalyst for ORR. This nanoparticle exhibited remarkably improved ORR activity in an alkaline electrolyte relative to the monometallic catalysts and showed superior material stability after an accelerated degradation test. In addition to the benefits of this catalytic material for ORR, this catalyst can be synthesized in only a few minutes via a surfactant-free microwave-assisted method. Hence, a facile and rapid preparation method has been established to attain clean and active catalyst surfaces free from surfactant residue, by which ORR is impeded.

Electrochemical properties of the Rh- and Sn-based catalysts were characterized using a rotating disk electrode in an oxygen-saturated 0.1 M potassium hydroxide solution, as shown in Figure 1a. Sn can be considered an ineffective catalyst for ORR in an alkaline electrolyte because carbon-supported Sn nanoparticles exhibited a polarization curve similar to that of the pure carbon support. Although the carbon-supported Rh nanoparticle had fair activity, it is not enough to be chosen as the suitable electrocatalyst for ORR. In terms of Rh–Sn catalyst (20 wt % of metal amounts, Figure S1), the atomic contents of Rh to Sn in the electrocatalyst were 72 and 28%, respectively, confirmed from inductively coupled plasma atomic emission spectroscopy results. This catalyst was denoted as Rh₃Sn₁/C, indicating a Rh:Sn atomic ratio of ~3:1 (Table S1). The Rh₃Sn₁/C catalyst showed remarkable improvements in ORR activity and onset potential compared to the monometallic catalysts (Figure S2a). In order to simply estimate the electrocatalytic ORR activity, the differences in half-wave potentials ($E_{1/2}$) were obtained. The Rh₃Sn₁/C catalyst showed positive shifts in $E_{1/2}$ of 120, 340, and 50 mV, relative to Rh/C, Sn/C, and commercial Pt/C, respectively. Kinetic current densities (i_k) in ORR curves at 0.75 and 0.80 V were calculated in accordance with Koutecky–Levich plots and are compared in Figure 1b.³⁴ Both Rh/C and Sn/C displayed extremely low kinetic current densities at those potentials, whereas the kinetic current density of Rh₃Sn₁/C exceeded them and was at least 5 times more than that of the commercial Pt/C catalyst. The

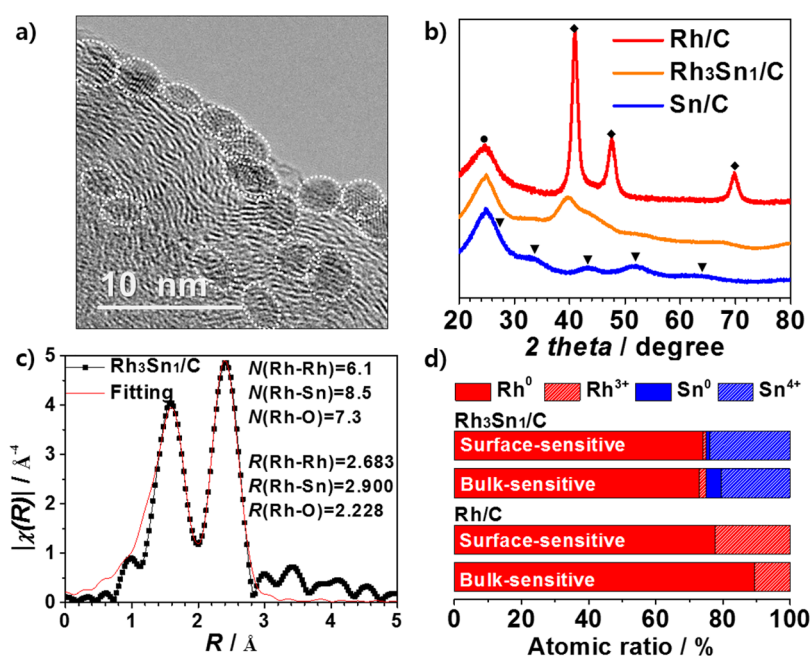


Figure 2. Morphological characteristics of Rh_3Sn_1 nanoparticles. (a) HR-TEM image of Rh_3Sn_1 nanoparticles on carbon support. (b) HR-XRD results for Rh/C , Sn/C and $\text{Rh}_3\text{Sn}_1/\text{C}$ (diamond: Rh, triangle: Sn/SnO_x, circle: carbon). (c) Fourier transform magnitudes of Rh K-edge EXAFS spectra for $\text{Rh}_3\text{Sn}_1/\text{C}$ catalyst. (d) Oxidation state information on Rh and Sn for Rh/C and $\text{Rh}_3\text{Sn}_1/\text{C}$ with XPS depth-profiling using incident photon energies of 630 and 1000 eV.

number of electrons transferred (n) during ORR can be also acquired (Figures 1c and S2b). The slopes are parallel at various potentials, demonstrating first-order reaction kinetics, and the number of electrons transferred for the $\text{Rh}_3\text{Sn}_1/\text{C}$ catalyst was 3.9–4.0, which implies almost complete electrocatalytic reduction of oxygen into water on the surface of the Rh–Sn nanoparticles. According to the Tafel plots in Figure 1d, the Rh–Sn nanoparticle catalyst had the lowest slope and the highest kinetic current density relative to the monometallic catalysts, which ensures superior charge-transfer kinetics of $\text{Rh}_3\text{Sn}_1/\text{C}$ for ORR catalysis in alkaline environment.

Figures 2a and S3 show that the Rh_3Sn_1 nanoparticles were uniformly distributed on the carbon support, as observed using high-resolution transmission electron microscopy (HR-TEM) combined with energy-dispersive X-ray spectroscopy (EDS). Each nanoparticle was evenly composed of Rh and Sn in the expected ratio, confirmed by a line-scanning technique of EDS measurement. The nanoparticles had an average diameter of 3.0 nm with a standard deviation of 0.4 nm. Such small deviation is due to the well-controlled nucleation and growth rates obtained through a microwave-assisted nanoparticle synthesis.³⁵ In order to reveal the crystal structure of the catalytic materials, high-resolution X-ray diffraction (HR-XRD) experiments were performed (Figure 2b). HR-XRD results for Rh/C and Sn/C verified the face-centered cubic structure of Rh and the tetragonal crystal structure of Sn and its oxide forms, respectively. For XRD data for $\text{Rh}_3\text{Sn}_1/\text{C}$, although a decrease in peak intensities was observed, ascribed to the phase transformation between face-centered cubic and tetragonal crystal structure, the diffraction peaks of Rh were found to shift to lower values without any splitting of the signals. This represents that the Rh–Sn alloy nanoparticles were successfully formed with lattice expansion. Fourier-transformed Rh K-edge extended X-ray absorption fine structure (EXAFS) is depicted in Figure 2c to identify the coordination chemistry of $\text{Rh}_3\text{Sn}_1/\text{C}$

C. The two main peaks are relevant to the first coordination shell of Rh, confirmed by simulation studies.³⁶ Coordination number of Rh–Rh for the Rh_3Sn_1 nanoparticle was 6.1, compared to 9.0 for pure Rh nanoparticles (Figure S4), indicating that Rh and Sn atoms were well-combined in an atomic scale rather than in the form of aggregates. High-resolution X-ray photoelectron spectroscopy (HR-XPS) was conducted to ascertain the relationship between catalytic activity and chemical composition of the catalysts. Surface and bulk sensitive information, especially the chemical states, can be determined by a depth-profiling technique with controlling incident photon energies based on the universal curve.³⁷ In spite of noble property of Rh, approximately one-fourth of the surface Rh atoms were oxidized for the Rh/C catalyst owing to a high surface-to-volume ratio of the nanoparticles (Figures 2d and S5). On the contrary, when Rh combined with Sn, most Rh atoms at the surface can be maintained as metallic Rh relative to the pure catalyst surface. Due to the difference in binding properties with oxygen species and metal, oxygen tends to bind with the adjacent Sn surface atom rather than with the Rh surface atom. Consequently, both catalysts secured similar contents of metallic Rh as an active site at their surfaces, even though one-fourth of Sn existed at the surface of $\text{Rh}_3\text{Sn}_1/\text{C}$. In addition to a preference for the oxidation of metal, the incorporation of Sn into the nanoparticle can induce a lateral repulsion by hydroxyl functional groups adsorbed on neighboring surface Sn atoms.³⁸ This leads to lower coverage of hydroxyl groups on the Rh surface atoms and retains clean and active surface with metallic Rh sites for easier adsorption of molecules. Furthermore, the reoxidation and removal of species adsorbed on Rh are also improved by adjacent hydroxyl groups adsorbed on Sn due to bifunctional effect.³⁹ Thus, tuning the nanoscale geometry of $\text{Rh}_3\text{Sn}_1/\text{C}$ can provide active surfaces and aggressive interactions, resulting in enhanced electrochemical

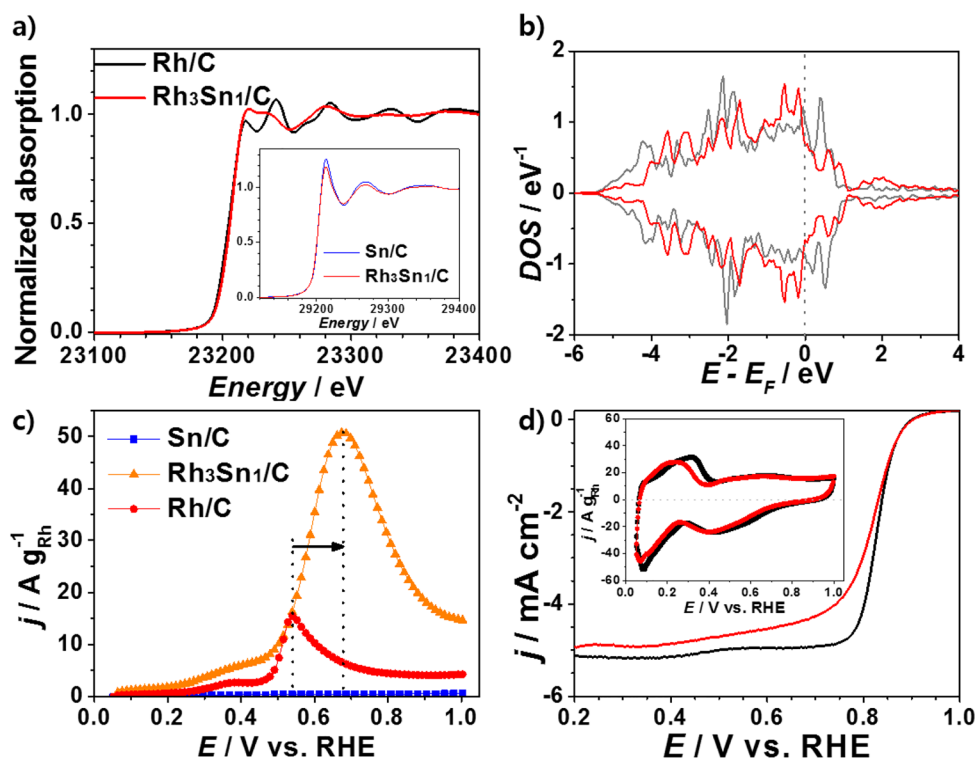


Figure 3. Characterizations of electronic structure and material stability for Rh_3Sn_1 nanoparticles. (a) Rh K-edge XANES results of Rh/C and $\text{Rh}_3\text{Sn}_1/\text{C}$. Inset: Sn K-edge XANES spectra for Sn/C and $\text{Rh}_3\text{Sn}_1/\text{C}$. (b) DFT calculations of density of states (DoS) for a surface Rh atom in Rh(111) (gray) and $\text{Rh}_3\text{Sn}_1(111)$ (red) planes. (The dotted line at 0 eV stands for a Fermi level.) (c) CO stripping measurement derived from CO displacement technique for Rh/C, Sn/C and $\text{Rh}_3\text{Sn}_1/\text{C}$. (d) Linear sweep voltammetry of $\text{Rh}_3\text{Sn}_1/\text{C}$ for the ORR before (black) and after (red) ADT of 3000 cycles. inset: Polarization curves of $\text{Rh}_3\text{Sn}_1/\text{C}$ before and after ADT in an oxygen-free 0.1 M potassium hydroxide at room temperature with a sweep rate of 20 mV s^{-1} .

activity toward ORR. Slight shifts in core-level binding energy for the $\text{Rh}_3\text{Sn}_1/\text{C}$ imply changes in electron configuration due to atomic-scale interactions between different metal atoms (Figure S5a–d).⁴⁰ It also suggests the idea of electronic modification supported by the following theoretical calculation and experiments.

In Figure 3a and its inset, the Rh K-edge and Sn K-edge X-ray absorption near-edge spectra for Rh/C, Sn/C, and $\text{Rh}_3\text{Sn}_1/\text{C}$ were displayed to determine their local symmetries. The first intense peak on Rh K-edge of $\text{Rh}_3\text{Sn}_1/\text{C}$ was increased, whereas that of Sn K-edge was diminished, signifying a decrease in the electron density of Rh. This leads to stronger interaction of adsorbates on the surface, resulting in lower adsorption energy barrier to bind with oxygen species.^{41,42} Density functional theory (DFT) is widely used to predict the trends on chemisorption, energy barrier, and dissociation of molecules on metal surfaces.^{43–45} With regard to the DFT studies, the electron density for two crystal planes, Rh(111) and $\text{Rh}_3\text{Sn}_1(111)$, were estimated along with their energy differences from a Fermi level (Figures 3b and S6). The crystal structure of Rh–Sn is assumed to be face-centered cubic for simplifying theoretical calculations, although it may exist in the phase transformation stage between the face-centered cubic structure of Rh and the tetragonal structure of Sn. According to the simulations at the $\text{Rh}_3\text{Sn}_1(111)$ surface, overall intensities of density of states shifted to higher energy values, which indicate a stronger interaction between a Rh surface atom of Rh_3Sn_1 and an adsorbed molecule.⁴⁶ With regard to the electrochemical experiments, the adsorption tendency of carbon monoxide (CO) on Rh surfaces with coordination number of metal atoms

is analogous to that of the oxygen species, and are in good agreement with the aforementioned theoretical calculations, as shown in Figure 3c.⁴⁷ CO displacement was achieved using the selective and irreversible adsorption ability of CO on Rh surface, and CO was subsequently oxidized to attain the extent of CO adsorption on Rh-based catalyst surfaces.⁴⁸ Upon incorporating Sn into Rh nanoparticles, the onset potential has a negative shift of 0.1 V relative to that of pure Rh/C, signifying that facile oxidation of CO molecules occurs at the interfacial regions due to the bifunctional effect. A positive shift of the intense peak from 0.54 V for the pure catalyst to 0.68 V was clearly observed, implying that CO adsorption is further strengthened at the Rh surface incorporated with Sn. Amounts of adsorbed CO also increased notably. Theoretical and experimental results supported stronger interaction of adsorbates with the surface Rh atom of Rh_3Sn_1 nanoparticles, caused by changes in electron configuration and coordination chemistry of the Rh atom. These electronic modifications may be derived from a decrease in coordination number with distortion of crystal structure, expansion of lattice parameters, and a nonlinearity between oxygen binding energy and Rh fraction in a nanoparticle.^{47,49–51} An accelerated degradation test (ADT) was assessed for 3000 potential cycles between 0.6 and 1.0 V at a scan rate of 50 mV s^{-1} to establish the long-term stability of the $\text{Rh}_3\text{Sn}_1/\text{C}$ catalyst (Figure 3d). Onset potentials near 0.90 V before and after ADT exhibited the same profiles, and thus, fair electrocatalytic activity after ADT was observed. Electrochemical surface areas (ECSAs) of the catalysts were also attained from the hydrogen desorption areas on cyclic voltammograms (inset, Figure 3d). The ECSA of fresh Rh/C

and fresh Rh₃Sn₁/C were revealed as 28.9 and 55.9 m²/g, respectively, attributed to the enhancement of catalyst utilization.⁵² Even a position of intense peak at regions of hydrogen desorption was negatively shifted after ADT, ECSA of Rh₃Sn₁/C was evaluated as 54.0 m²/g. This implies only slight morphological changes on the Rh₃Sn₁/C surface under harsh operating conditions, due to the electrocatalyst design with corrosion-resistant nanomaterial.

Facile synthesis of a new type of Rh–Sn nanoparticle is presented to achieve a highly active and stable ORR electrocatalyst. Electrocatalytic activity of the Rh₃Sn₁/C catalyst is ascribed to providing clean and active surface Rh sites by lateral repulsion and a bifunctional mechanism, as well as evolution of sufficient interacting systems between the adsorbates and the metal atoms by electronic modification. Nanoscale Rh–Sn combination also contributes to the improvement of catalyst utilization. Furthermore, corrosion-resistant ability of Rh contributes to the stable structure of the Rh–Sn nanoparticle, which endures well under harsh operating conditions. In addition to superior catalytic properties, the surfactant-free microwave-assisted method presented here results in rapid synthesis of the Rh–Sn nanoparticles in a few minutes without any further treatment steps to eradicate surface-capped organic molecules. It is ascertained that these procedures and material designs produce highly active and stable cost-effective catalysts for ORR. Future efforts are focused on other combined electrocatalytic systems including combination of non-Pt (or Pd) metal and transition metal, which create valuable materials based on theoretical and experimental approaches in the fields of nanomaterials and electrocatalysis.

■ ASSOCIATED CONTENT

Supporting Information

The Supporting Information is available free of charge on the ACS Publications website at DOI: 10.1021/acscatal.7b02402.

Text and figures giving details of Rh–Sn nanoparticle experimental synthesis; morphological, structural, and electrochemical characterization data; and detailed information about DFT calculations (PDF)

■ AUTHOR INFORMATION

Corresponding Authors

*E-mail for S.J.Y.: ysj@kist.re.kr.

*E-mail for Y.-E.S.: ysung@snu.ac.kr.

ORCID

Hyung Chul Ham: 0000-0003-0850-584X

Yung-Eun Sung: 0000-0002-1563-8328

Sung Jong Yoo: 0000-0003-1556-0206

Notes

The authors declare no competing financial interest.

■ ACKNOWLEDGMENTS

This work was supported by the Global Frontier R&D Program on Center for Multiscale Energy System funded by NRF (2016M3A6A7945505), the KIST Institutional Program, and the NRF grant funded by MSIP (2017R1A2B2003363). This work was also supported by the New & Renewable Energy Core Technology Program of KETEP, granted financial resource from MOTIE, Republic of Korea (20143030031340).

■ REFERENCES

- (1) Debe, M. K. *Nature* **2012**, *486*, 43–51.
- (2) Xia, W.; Mahmood, A.; Liang, A. Z.; Zou, R.; Guo, S. *Angew. Chem., Int. Ed.* **2016**, *55*, 2650–2676.
- (3) Shao, M.; Chang, Q.; Dodelet, J.-P.; Chenitz, R. *Chem. Rev.* **2016**, *116*, 3594–3657.
- (4) Markovic, N. M.; Gasteiger, H. A.; Ross, P. N., Jr. *J. Phys. Chem.* **1995**, *99*, 3411–3415.
- (5) Jiang, K.; Wang, P.; Guo, S.; Zhang, X.; Shen, X.; Lu, G.; Su, D.; Huang, X. *Angew. Chem., Int. Ed.* **2016**, *55*, 9030–9035.
- (6) Stephens, I. E. L.; Bondarenko, A. S.; Grønberg, U.; Rossmeisl, J.; Chorkendorff, I. *Energy Environ. Sci.* **2012**, *5*, 6744–6762.
- (7) Ge, X.; Sumboja, A.; Wu, D.; An, T.; Li, B.; Goh, F. W. T.; Hor, T. S. A.; Zong, Y.; Liu, Z. *ACS Catal.* **2015**, *5*, 4643–4667.
- (8) Stamenkovic, V. R.; Mun, B. S.; Arenz, M.; Mayrhofer, K. J. J.; Lucas, C. A.; Wang, G.; Ross, P. N.; Markovic, N. M. *Nat. Mater.* **2007**, *6*, 241–247.
- (9) Greeley, J.; Stephens, I. E. L.; Bondarenko, A. S.; Johansson, T. P.; Hansen, H. A.; Jaramillo, T. F.; Rossmeisl, J.; Chorkendorff, I.; Nørskov, J. K. *Nat. Chem.* **2009**, *1*, 552–556.
- (10) Yoo, S. J.; Hwang, S. J.; Lee, J.-G.; Lee, S.-C.; Lim, T.-H.; Sung, Y.-E.; Wieckowski, A.; Kim, S.-K. *Energy Environ. Sci.* **2012**, *5*, 7521–7525.
- (11) Stamenkovic, V. R.; Fowler, B.; Mun, B. S.; Wang, G.; Ross, P. N.; Lucas, C. A.; Markovic, N. M. *Science* **2007**, *315*, 493–497.
- (12) Lai, J.; Luque, R.; Xu, G. *ChemCatChem* **2015**, *7*, 3206–9228.
- (13) Alia, S. M.; Jensen, K.; Contreras, C.; Garzon, F.; Pivovar, B.; Yan, Y. *ACS Catal.* **2013**, *3*, 358–362.
- (14) Han, S.; Chae, G.-S.; Lee, J. S. *Korean J. Chem. Eng.* **2016**, *33*, 1799–1804.
- (15) Cui, C.; Gan, L.; Heggen, M.; Rudi, S.; Strasser, P. *Nat. Mater.* **2013**, *12*, 765–771.
- (16) Baldizzone, C.; Gan, L.; Hodnik, N.; Keeley, G. P.; Kostka, A.; Heggen, M.; Strasser, P.; Mayrhofer, K. J. J. *ACS Catal.* **2015**, *5*, 5000–5007.
- (17) Rabis, A.; Rodriguez, P.; Schmidt, T. J. *ACS Catal.* **2012**, *2*, 864–890.
- (18) Wu, Y.; Wang, D.; Zhou, G.; Yu, R.; Chen, C.; Li, Y. *J. Am. Chem. Soc.* **2014**, *136*, 11594–11597.
- (19) Erini, N.; Rudi, S.; Beermann, V.; Krause, P.; Yang, R.; Huang, Y.; Strasser, P. *ChemElectroChem* **2015**, *2*, 903–908.
- (20) Huang, X.; Zhao, Z.; Cao, L.; Chen, Y.; Zhu, E.; Lin, Z.; Li, M.; Yan, A.; Zettl, A.; Wang, Y. M.; Duan, X.; Mueller, T.; Huang, Y. *Science* **2015**, *348*, 1230–1234.
- (21) Narayanamoorthy, B.; Balaji, S.; Sita, C.; Pasupathi, S.; Eswaramoorthy, M.; Moon, I.-S. *ACS Sustainable Chem. Eng.* **2016**, *4*, 6480–6490.
- (22) Chen, W.; Ny, D.; Chen, S. J. *Power Sources* **2010**, *195*, 412–418.
- (23) Yan, Y.; Zhan, F.; Du, J.; Jiang, Y.; Jin, C.; Fu, M.; Zhang, H.; Yang, D. *Nanoscale* **2015**, *7*, 301–307.
- (24) Qi, Y.; Wu, J.; Zhang, H.; Jiang, Y.; Jin, C.; Fu, M.; Yang, H.; Yang, D. *Nanoscale* **2014**, *6*, 7012–7018.
- (25) Nakada, M.; Ishihara, A.; Mitsushima, S.; Kamiya, N.; Ota, K. *Electrochem. Solid-State Lett.* **2007**, *10*, F1–F4.
- (26) Zhu, M.; Sun, G.; Xin, Q. *Electrochim. Acta* **2009**, *54*, 1511.
- (27) Breiter, M. W. *Electrochim. Acta* **1963**, *8*, 973–983.
- (28) Aramata, A.; Toyoshima, I.; Enyo, M. *Electrochim. Acta* **1992**, *37*, 1317–1320.
- (29) Du, W.; Wang, Q.; Saxner, D.; Deskins, N. A.; Su, D.; Krzanowski, J. E.; Frenkel, A. I.; Teng, X. *J. Am. Chem. Soc.* **2011**, *133*, 15172–15183.
- (30) Ahn, M.; Cha, I. Y.; Lee, J. K.; Yoo, S. J.; Sung, Y.-E. *J. Mater. Chem. A* **2015**, *3*, 17130–17134.
- (31) Zhang, N.; Chen, X.; Lu, Y.; An, L.; Li, X.; Xia, D.; Zhang, Z.; Li, J. *Small* **2014**, *10*, 2662–2669.
- (32) Xie, S.; Lu, N.; Xie, Z.; Wang, J.; Kim, M. J.; Xia, Y. *Angew. Chem., Int. Ed.* **2012**, *51*, 10266–10270.

- (33) Sneed, B. T.; Brodsky, C. N.; Kuo, C.-H.; Lamontagne, L. K.; Jiang, Y.; Wang, Y.; Tao, F.; Huang, W.; Tsung, C.-K. *J. Am. Chem. Soc.* **2013**, *135*, 14691–14700.
- (34) Wang, D.; Xin, H. L.; Hovden, R.; Wang, H.; Yu, Y.; Muller, D. A.; DiSalvo, F. J.; Abruna, H. D. *Nat. Mater.* **2012**, *12*, 81–87.
- (35) Baghbanzadeh, M.; Carbone, L.; Cozzoli, P. D.; Kappe, C. O. *Angew. Chem., Int. Ed.* **2011**, *50*, 11312–11359.
- (36) Becknell, N.; Kang, Y.; Chen, C.; Resasco, J.; Kornienko, N.; Guo, J.; Markovic, N. M.; Somorjai, G. A.; Stamenkovic, V. R.; Yang, P. *J. Am. Chem. Soc.* **2015**, *137*, 15817–15824.
- (37) Seah, M. P.; Dench, W. A. *Surf. Interface Anal.* **1979**, *1*, 2–11.
- (38) Zhang, J.; Vukmirovic, M. B.; Sasaki, K.; Nilekar, A. U.; Mavrikakis, M.; Adzic, R. R. *J. Am. Chem. Soc.* **2005**, *127*, 12480–12481.
- (39) Antolini, E.; Gonzalez, E. R. *Catal. Today* **2011**, *160*, 28–38.
- (40) Tan, X.; Wang, L.; Zahiri, B.; Kohandehghan, A.; Karpuzov, D.; Lotfabad, E. M.; Li, Z.; Eikerling, M. H.; Mitlin, D. *ChemSusChem* **2015**, *8*, 361–376.
- (41) Russell, A. E.; Rose, A. *Chem. Rev.* **2004**, *104*, 4613–4636.
- (42) Jeon, T.-Y.; Yoo, S. J.; Cho, Y.-H.; Lee, K.-S.; Kang, S. H.; Sung, Y.-E. *J. Phys. Chem. C* **2009**, *113*, 19732–19739.
- (43) Greeley, J.; Mavrikakis, M. *Nat. Mater.* **2004**, *3*, 810–815.
- (44) Norskov, J. K.; Rossmeisl, J.; Logadottir, A.; Lindqvist, L.; Kitchin, J. R.; Bligaard, T.; Jonsson, H. *J. Phys. Chem. B* **2004**, *108*, 17886–17892.
- (45) Anderson, A. B.; Jinnouchi, R.; Uddin, J. *J. Phys. Chem. C* **2013**, *117*, 41–48.
- (46) Hwang, S. J.; Kim, S.-K.; Lee, J.-G.; Lee, S.-C.; Jang, J. H.; Kim, P.; Lim, T.-H.; Sung, Y.-E.; Yoo, S. J. *J. Am. Chem. Soc.* **2012**, *134*, 19508–19511.
- (47) Peterson, A. A.; Grabow, L. C.; Brennan, T. P.; Shong, B.; Ooi, C.; Wu, D. M.; Li, C. W.; Kushwaha, A.; Medford, A. J.; Mbuga, F.; Li, L.; Norskov, J. K. *Top. Catal.* **2012**, *55*, 1276–1282.
- (48) Ferrando, R.; Jellinek, J.; Johnston, R. L. *Chem. Rev.* **2008**, *108*, 845–910.
- (49) Gonzalez, S.; Sousa, C.; Illas, F. *Surf. Sci.* **2003**, *531*, 39–52.
- (50) Tang, W.; Zhang, L.; Henkelman, G. *J. Phys. Chem. Lett.* **2011**, *2*, 1328–1331.
- (51) Wu, J.; Shan, S.; Luo, J.; Joseph, P.; Petkov, V.; Zhong, C.-J. *ACS Appl. Mater. Interfaces* **2015**, *7*, 25906–25913.
- (52) Liu, Y.; Xu, C. *ChemSusChem* **2013**, *6*, 78–84.